

Two-dimensional Paired Topological Superfluids of Rydberg Fermi Gases

Ching-Yu Huang,¹ Jiapei Zhuang,² Po-Yao Chang,² and Daw-Wei Wang^{3,4,5,6}

¹*Department of Applied Physics, Tunghai University, Taichung 40704, Taiwan*

²*Department of Physics, National Tsing Hua University, Hsinchu 30013, Taiwan*

³*Department of Physics, National Tsing Hua University, Hsinchu 30013, Taiwan*

⁴*Physics Division, National Center for Theoretical Sciences, Taipei 10617, Taiwan*

⁵*Frontier Center for Theory and Computation, National Tsing Hua University, Hsinchu 30013, Taiwan*

⁶*Center for Quantum Technology, National Tsing Hua University, Hsinchu 30013, Taiwan*

(Dated: December 30, 2021)

We systematically investigate the topological properties of spin polarized Rydberg-dressed fermionic atoms loaded in a bilayer optical lattice. Through tuning the Rydberg coupling strength and the inter-layer tunneling amplitude, we identify different types of topological superfluid states generated from the inter-layer pairing and relative gauge phase modulation of the couples 2D p -wave superfluids. These phases includes gapped/gapless with/without time reversal symmetry. One of the most interesting states is a gapless paired topological superfluid with both the time-reversal symmetry and particle-hole symmetry. This state is equivalent to a topological Kondo lattice model with the spin-orbit coupling, an in-plane magnetic field, and an additional particle-hole symmetry [1]. The flexibility of experimental manipulation in such Rydberg-dressed fermionic systems therefore becomes a promising system for realizing interesting topological superfluids.

I. INTRODUCTION

A Majorana fermion is defined to be its own antiparticle [2], and is a hypothetical particle in the theoretical high energy physics. In condensed matter systems, a Majorana fermion can appear as a localized edge state, reflecting the topological feature in the bulk of system. It is known that systems with topological feature can be classified as the symmetry-protected topological (SPT) orders, which are robust against local perturbations for a given on-site symmetries [3]. Ground states of nontrivial SPT phases cannot be continuously connected to trivial product states without either closing the gap or breaking the protecting symmetry [4]. One of the mostly studied SPT phases is proposed by Kitaev [5] for one-dimensional (1D) p -wave superconductor. The Majorana zero mode (MZM) of such system may be applied for quantum computation through braiding, and certain experimental signature has been proposed in an ordinary s -wave superconducting wire with strong spin-orbital coupling through proximity effect [6–14] or even in systems of ultracold atoms [15–18]. However non-ambiguous evidence is still lacking probably due to the poor signal-to-noise ratio for a localized MZM. Recently, some extensions of Kitaev’s 1D model by including inter-chain tunneling [19], dimerization [20], and long-ranged pairing [21, 22] have also been proposed.

To stabilize interesting phases (nematic states, classical crystals, or quantum solids) in condensed matter systems, the interactions are required to be strong enough to compete with the Fermi energy. One have to search and synthesize strongly correlated materials, which is a difficult task. On the other hand, the Rydberg atoms provide a better playground for investigating interesting phases from its highly tunability. E.g., the length scale and strength of the effective inter-atom interaction can be manipulated easily by external fields [23–27]. In addition to the blockade effect for on-resonant excitations [28–31], one can also apply a far-detuned weak field to generate an effective Rydberg-dressed interaction (RDI), which has a soft core and a finite interaction range ([32–34]. The-

oretical calculations show that a repulsive RDI in a Bose gas may lead to a supersolid droplet phase [32, 33, 35–37], while an attractive RDI induces a 3D bright soliton [38]. For a Rydberg Fermi gas, some topological phases are also predicted for an attractive [39] or repulsive interaction in an optical lattice near half-filling [40]. Recently, Rydberg-dressed effective interaction has been observed for two individually trapped atoms [41] and in a 2D optical lattice by measuring the spin correlation [42].

$t_z = 0$	$\phi_{\uparrow/\downarrow} = 0$	$\phi_{\uparrow/\downarrow} = \pi/2$	$\phi_{\uparrow/\downarrow} = 0/\pi$
$\alpha_{\uparrow/\downarrow} = 0$	○	○	○
$\alpha_{\uparrow/\downarrow} = 0/\pi$	×*	○	○
$t_z \neq 0$	$\phi_{\uparrow/\downarrow} = 0$	$\phi_{\uparrow/\downarrow} = \pi/2$	$\phi_{\uparrow/\downarrow} = 0/\pi$
$\alpha_{\uparrow/\downarrow} = 0$	○	○	×
$\alpha_{\uparrow/\downarrow} = 0/\pi$	×	×	×#

TABLE I. The 12 representative cases and their types classified by their parameters and associate energy gap. ○ indicates gapped spectrum and × indicates the gapless spectrum. * and # are two cases discussed in main text. The former one preserves both the time-reversal symmetry and the particle-hole symmetry [symmetry class DIII], and the later one only preserves the particle-hole symmetry [symmetry class D].

In this paper, we systematically study the topological properties of the ground states of fermionic Rydberg atoms loaded in a bilayer optical lattice. The effective Rydberg-dressing interaction is tuned to be attractive in all directions and hence generates the in-plane pairing (Δ_x^σ and Δ_y^σ) as well as the inter-layer pairing (Δ_z) at the same time (here $\sigma = \uparrow, \downarrow$ stands for the upper/lower layer index). Similar to the emergent gapless phases induced by inversion symmetry breaking in three dimensions [43], the transitions between two topological phases might go through gapless phases. In this work, we focus on the topological properties of gapless phases. We first find that the topological properties of the ground state also de-

pend not only on the system parameters, but also depend on the relative gauges phases between these order parameters. By calculating the entanglement spectrum, topological charge of the gapless points, and eigenstate energy/wavefunctions of a finite size systems, we identify two types of interesting gapless phases as follows. **Type I**: the topological gapless phase with the particle-hole symmetry (\mathcal{P}), belonging to symmetry class D. **Type II**: the topological gapless phase with both the time-reversal symmetry (\mathcal{T}) and the particle-hole symmetry (\mathcal{P}) belonging to symmetry class DIII. The Type I phase further breaks the C_4 in-plane rotational lattice symmetry, making different zero energy flat bands in x and y directions. We also find that Type II phase could be mapped onto a topological Kondo lattice models with spin-orbital coupling, an external magnetic field, and an additional particle-hole symmetry [1]. The paired topological superfluids studied here is therefore a quiet general and practical system for the investigation of many interesting topological properties. These phases are summarized in Table I.

The manuscript is organized as follows: In Sec. II we briefly describe the physical system of Rydberg atoms in 2D bilayer optical lattice. We derive the effective mean-field Hamiltonian and discuss their symmetry properties. In Sec. III we explain how to detect the topological properties using entanglement spectrum/entropy as well as finite size calculation. We then show our calculation results for the two types of phases in Sec. IV A and Sec. IV B. We then provide further discussion in Sec. V and conclude our paper in Sec. VI. In Appendix A, we explicitly calculate the single-particle energy spectra of mean-field Hamiltonian.

II. PHYSICAL SYSTEM, MODEL HAMILTONIAN, AND SYMMETRY PROPERTIES

A. Effective Interaction

We consider a single-species Fermi gas, where each atom is weakly coupled to its Rydberg excited state by an off-resonant two photon transition via an intermediate state. In the far detuning and weak coupling limit, we can apply the standard perturbation and adiabatic approximation [32] and obtain the effective Rydberg-dressed interaction between dressed state atoms: $V_{\text{RD}}(\mathbf{r}) = \frac{U_0}{1+(r/R_c)^6}$ [33, 38, 39, 44], where Ω and Δ are the effective Raman coupling and detuning respectively. $U_0 \equiv (\Omega/2\Delta)^4 C_6/R_c^6$, and $R_c \equiv (C_6/2|\Delta|)^{1/6}$ are the interaction strength and the averaged soft-core radius (Rydberg blockade radius). C_6 is the averaged van der Waals coefficient, which can be shown to be negative ($U_0 < 0$) for all orbital states when exciting 6Li to a $|nD\rangle$ state with $n > 30$ [45, 46]. Note that the radius R_c could be tuned by the external laser detuning and strength independently by keeping the total interaction amplitude (U_0) the same. The decay rate of the two-photon process can be strongly reduced by choosing larger detuning in the first transition, and the atomic loss rate due to the orbital level crossing in the short-distance can be also reduced by Pauli exclusion principle. More details of possible experimental setting can be found in Ref. [39].

B. Mean field Hamiltonian in real space

The full system Hamiltonian for spin polarized Rydberg Fermi gas in a 2D bilayer optical lattice can be expressed as follows in the real-space coordinates:

$$H = - \sum_{\mathbf{r}, \sigma=\uparrow, \downarrow} \left[\mu c_{\mathbf{r}, \sigma}^\dagger c_{\mathbf{r}, \sigma} + t c_{\mathbf{r}, \sigma}^\dagger c_{\mathbf{r}+\hat{x}, \sigma} + t c_{\mathbf{r}, \sigma}^\dagger c_{\mathbf{r}+\hat{y}, \sigma} \right] - t_z \sum_{\mathbf{r}} c_{\mathbf{r}, \uparrow}^\dagger c_{\mathbf{r}, \downarrow} + h.c. \quad (1)$$

$$+ \frac{1}{2} \sum_{\mathbf{r}, \mathbf{r}'} \left[V_{\parallel}(\mathbf{r} - \mathbf{r}') \left(c_{\mathbf{r}, \uparrow}^\dagger c_{\mathbf{r}', \uparrow}^\dagger c_{\mathbf{r}', \uparrow} c_{\mathbf{r}, \uparrow} + c_{\mathbf{r}, \downarrow}^\dagger c_{\mathbf{r}', \downarrow}^\dagger c_{\mathbf{r}', \downarrow} c_{\mathbf{r}, \downarrow} \right) + V_{\perp}(\mathbf{r} - \mathbf{r}') \left(c_{\mathbf{r}, \uparrow}^\dagger c_{\mathbf{r}', \downarrow}^\dagger c_{\mathbf{r}', \downarrow} c_{\mathbf{r}, \uparrow} + c_{\mathbf{r}, \downarrow}^\dagger c_{\mathbf{r}', \uparrow}^\dagger c_{\mathbf{r}', \uparrow} c_{\mathbf{r}, \downarrow} \right) \right]$$

where $c_{\mathbf{r}}^\dagger (c_{\mathbf{r}, \sigma})$ is the creation (annihilation) operator of fermions for the layer index σ and the in-plane coordinate $\mathbf{r} = (i_x, i_y)$. μ , t and t_z are the chemical potential, the intralayer hopping amplitude, and the inter-layer hopping amplitude. $V_{\perp}(\mathbf{r} - \mathbf{r}')$ and $V_{\parallel}(\mathbf{r} - \mathbf{r}')$ are the interlayer and intralayer interaction, respectively.

In order to simplify the system for a concrete discussion and comparison, below we will consider the situation when the Rydberg blockade radius, R_c , is tuned to be close to the in-plane lattice spacing, a , and the interlayer distance, d , so that only the nearest neighboring attractive interaction are considered throughout this paper. Extension to longer range interaction could be also carried out easily, but we believe all the quantitative results we discuss below will not change.

By considering the nearest-neighboring-site interaction only, we could simply obtain the following mean-field Hamil-

tonian by introducing the nearest neighboring coupling:

$$H = \sum_{\mathbf{r}, \sigma=\uparrow, \downarrow} \left[- \mu c_{\mathbf{r}, \sigma}^\dagger c_{\mathbf{r}, \sigma} - t c_{\mathbf{r}, \sigma}^\dagger c_{\mathbf{r}+\hat{x}, \sigma} - t c_{\mathbf{r}, \sigma}^\dagger c_{\mathbf{r}+\hat{y}, \sigma} \right. \\ \left. + \Delta_x^\sigma c_{\mathbf{r}, \sigma}^\dagger c_{\mathbf{r}+\hat{x}, \sigma} + i \Delta_y^\sigma c_{\mathbf{r}, \sigma}^\dagger c_{\mathbf{r}+\hat{y}, \sigma} + h.c. \right] \quad (2)$$

$$+ \sum_{\mathbf{r}} \left[- t_z c_{\mathbf{r}, \uparrow}^\dagger c_{\mathbf{r}, \downarrow} + \Delta_z c_{\mathbf{r}, \uparrow}^\dagger c_{\mathbf{r}, \downarrow} + h.c. \right] + \text{const.}$$

Here Δ_z is the gap function between the upper (\uparrow) and bottom layer (\downarrow) on site \mathbf{r} , and $\Delta_{x(y)}^\sigma$ are the gap function between the nearest-neighboring sites for $\sigma = \uparrow, \downarrow$ layers. More precisely,

we have

$$\begin{aligned}\Delta_x^\sigma &= e^{i\phi_\sigma} \Delta_p \equiv V_{\parallel}(\hat{x}) \langle c_{\mathbf{r}+\hat{x},\sigma} c_{\mathbf{r},\sigma} \rangle \\ \Delta_y^\sigma &= e^{i\alpha_\sigma} e^{i\phi_\sigma} \Delta_p \equiv V_{\parallel}(\hat{y}) \langle c_{\mathbf{r}+\hat{y},\sigma} c_{\mathbf{r},\sigma} \rangle, \\ \Delta_z &= \Delta_s \equiv V_{\perp}(\mathbf{r}-\mathbf{r}') \langle c_{\mathbf{r},\downarrow} c_{\mathbf{r},\uparrow} \rangle.\end{aligned}\quad (3)$$

Here the four phases $\alpha_{\uparrow,\downarrow}$ and $\phi_{\uparrow,\downarrow}$ are all arbitrary by fixing the gauge phase of the inter-layer pairing, $\Delta_z \equiv \Delta_s$. We have set Δ_p and Δ_s are both real and positive. The phase difference between Δ_x^σ and Δ_y^σ makes the system different from the ordinary $p_x \pm ip_y$ pairing system, and may generate interesting topological properties as we will study later. Throughout this paper, we set $\Delta_z = \Delta_s$ to be real and positive in order to fix the overall gauge phase.

C. Mean-field Hamiltonian in momentum space

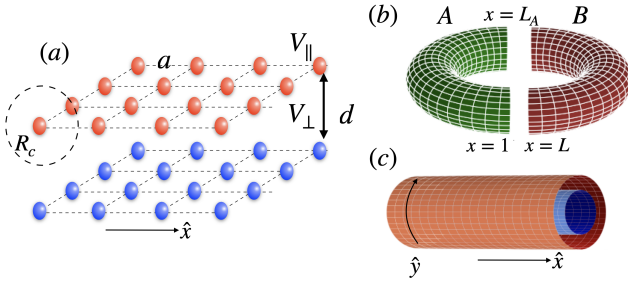


FIG. 1. (a) The schematic figure for the system investigated in this paper: Rydberg-dressing spin-polarized fermions are loaded into a bilayer system with an in-plane square optical lattice. The Rydberg-dressing amplitude and radius, R_c , could be manipulated in a wide range of laser detuning and Rabi coupling strength. Here we just consider the case when R_c is similar to the in-plane lattice constant (a) and inter-layer spacing (d), so that only the nearest neighbouring interaction, V_{\parallel} , and the inter-layer on-site interaction, V_{\perp} , are included in the Hamiltonian for simplicity. (b) The torus generated by the periodic boundary condition in both x and y direction of the bilayer system. When we consider the edge mode with an open boundary condition in x axis, we cut the torus by keeping periodic boundary condition in the y direction. As a result, the system becomes equivalent to two co-centered “finite cylinders” as shown in (c). After introducing the mean-field pairing and the Fourier transform along the y direction, Hamiltonian becomes equivalent to a 4-leg ladder with the index $\pm k_y$ and $\sigma = \uparrow / \downarrow$, which could then be diagonalized easily to get the full energy spectrum as well as the edge mode at the boundary of the x axis. See the text for more details.

We analyze the mean-field Hamiltonian both for the periodic boundary condition and the open boundary condition. The former provides the band structure properties in the bulk while the later reveals the existence of possible topological protected boundary states. To investigate the bulk properties with the periodic boundary condition, we transform the field operators as $c_{\mathbf{r},\sigma} = \frac{1}{N} \sum_{\mathbf{k}} c_{\mathbf{k},\sigma} e^{i\mathbf{r}\cdot\mathbf{k}}$ with $\mathbf{r} = (i_x, i_y)$, $\mathbf{k} = (k_x, k_y)$ and N being the total number of lattice sites in the 2D plane. The resulting Hamiltonian can be expressed to

be (after neglecting a constant term) $H = \sum_{\mathbf{k}} \Psi_{\mathbf{k}}^\dagger H(\mathbf{k}) \Psi_{\mathbf{k}}$ with

$$H(\mathbf{k}) = \begin{pmatrix} \varepsilon_{\mathbf{k}} & -t_z & (\tilde{\Delta}_{\mathbf{k}}^\uparrow)^\dagger & \Delta_s \\ -t_z & \varepsilon_{\mathbf{k}} & -\Delta_s & (\tilde{\Delta}_{\mathbf{k}}^\downarrow)^\dagger \\ \tilde{\Delta}_{\mathbf{k}}^\uparrow & -\Delta_s & -\varepsilon_{\mathbf{k}} & t_z \\ \Delta_s & \tilde{\Delta}_{\mathbf{k}}^\downarrow & t_z & -\varepsilon_{\mathbf{k}} \end{pmatrix} = \begin{pmatrix} H_0 & H_1^\dagger \\ H_1 & -H_0 \end{pmatrix} \quad (4)$$

and the Nambu spinor $\Psi_{\mathbf{k}} \equiv (c_{\mathbf{k},\uparrow}, c_{\mathbf{k},\downarrow}, c_{-\mathbf{k},\uparrow}^\dagger, c_{-\mathbf{k},\downarrow}^\dagger)^T$. Here we have defined

$$\begin{aligned}\varepsilon_{\mathbf{k}} &= -\mu - 2t \cos k_x - 2t \cos k_y, \\ \tilde{\Delta}_{\mathbf{k}}^\sigma &= 2ie^{i\phi_\sigma} \Delta_p (\sin k_x + ie^{i\alpha_\sigma} \sin k_y).\end{aligned}\quad (5)$$

and

$$H_0 = \begin{pmatrix} \varepsilon_{\mathbf{k}} & -t_z \\ -t_z & \varepsilon_{\mathbf{k}} \end{pmatrix} = \varepsilon_{\mathbf{k}} \sigma_0 - t_z \sigma_x \quad (6)$$

$$H_1 = \begin{pmatrix} \tilde{\Delta}_{\mathbf{k}}^\uparrow & -\Delta_s \\ \Delta_s & \tilde{\Delta}_{\mathbf{k}}^\downarrow \end{pmatrix} = i(\Delta_s \sigma_0 + \Delta_p \mathbf{d}_{\mathbf{k}} \cdot \vec{\sigma}) \times \sigma_y \quad (7)$$

where $\sigma_0 = I$ and σ_α ($\alpha = x, y, z$) are Pauli matrices. The general form of the effective magnetic field, $\mathbf{d}_{\mathbf{k}}$, can be very complicated. Here we show three typical $\mathbf{d}_{\mathbf{k}}$ that we will discuss in details in the following sections:

$$\begin{aligned}\mathbf{d}_{\mathbf{k}} &= (0, 2 \sin k_x + 2i \sin k_y, 0), & (\alpha_{\uparrow/\downarrow}, \phi_{\uparrow/\downarrow}) &= (0, 0), \\ \mathbf{d}_{\mathbf{k}} &= (2 \sin k_y, 2 \sin k_x, 0), & (\alpha_{\uparrow/\downarrow}, \phi_{\uparrow/\downarrow}) &= (0, 0/\pi), \\ \mathbf{d}_{\mathbf{k}} &= (-2i \sin k_x, 2i \sin k_y, 0), & (\alpha_{\uparrow/\downarrow}, \phi_{\uparrow/\downarrow}) &= (0/\pi, 0/\pi).\end{aligned}\quad (8)$$

One should notice that the above Bogoliubov–de Gennes (BdG) Hamiltonian is similar to the noncentrosymmetric superconductors [47–49]. Due to the lack of inversion symmetry, odd and even pairings are mixed and the BdG Hamiltonian can be gapless.

D. The system symmetry

Now we examine the symmetry class of the Hamiltonian by considering the time-reversal symmetry (\mathcal{T}), and the particle-hole symmetry (\mathcal{P}), chiral symmetry (\mathcal{C}) in the original BdG Hamiltonian. They are respectively defined as,

$$\begin{aligned}\mathcal{T} H(\mathbf{k}) \mathcal{T}^\dagger &= H^*(-\mathbf{k}) \\ \mathcal{P} H(\mathbf{k}) \mathcal{P}^\dagger &= -H^T(-\mathbf{k}) \\ \mathcal{C} H(\mathbf{k}) \mathcal{C}^\dagger &= -H(\mathbf{k})\end{aligned}\quad (9)$$

Within the spinor representation, the first three symmetry operations could be also expressed by Pauli matrix in the isospin basis as following:

$$\begin{aligned}\mathcal{T} &= \sigma_0 \otimes i\sigma_y, & \mathcal{T}^2 &= -1 \\ \mathcal{P} &= \sigma_x \otimes \sigma_0, & \mathcal{P}^2 &= 1 \\ \mathcal{C} &= \mathcal{P}\mathcal{T}^\dagger = (\sigma_x \otimes \sigma_0)(\sigma_0 \otimes -i\sigma_y)\end{aligned}\quad (10)$$

We note that unlike the chiral superconductor with $p_x + ip_y$ pairing which breaks the time-reversal symmetry, the bilayer system we study here provides a possibility of the time-reversal symmetric state. More precisely, we find that for $t_z = 0$, $\phi_\uparrow = -\phi_\downarrow$ and $\alpha_\uparrow = \pi + \alpha_\downarrow$, the mean-field Hamiltonian is time-reversal invariant, $\mathcal{T}H(\mathbf{k})\mathcal{T}^\dagger = H^*(-\mathbf{k})$. In other words, the chiral directions of the two superfluids in the upper and lower layers are opposite, making the time-reversal symmetry restored if reversing the parity in the z axis. Furthermore, we show that after a unitary transformation, the time-reversal symmetric case with $t_z = 0$, $\phi_\uparrow = \phi_\downarrow = 0$, $\alpha_\uparrow = 0$, and $\alpha_\downarrow = \pi$ could be exactly mapped onto a topological Kondo lattice model with spin-orbital coupling, an external magnetic field, and an additional particle-hole symmetry [1]. On the other hand, our model is defined on the square lattice with the C_4 in-plane rotational lattice symmetry (\mathcal{C}_4).

In the rest of this paper, we always consider the cases when Δ_s and Δ_p are finite but with different combination of t_z , $\alpha_{\uparrow/\downarrow}$ and $\phi_{\uparrow/\downarrow}$. More precisely, we consider the following $2 \times 2 \times 2 = 12$ representative system parameters with 2 values of t_z ($= 0$ or $\neq 0$), 2 values of $(\alpha_\uparrow, \alpha_\downarrow)$ ($= (0, 0)$ or $= (0, \pi)$), and 3 values of $(\phi_\uparrow, \phi_\downarrow)$ ($= (0, 0)$, $= (\pi/2, \pi/2)$ or $= (0, \pi)$). Moreover, we observe several gapless phases in our mean-field Hamiltonian. In particular, we only show two cases describing gapless phases with two values of t_z ($= 0$ or $\neq 0$) by fixed $(\phi_\uparrow, \phi_\downarrow) = (0, 0)$ and $(\alpha_\uparrow, \alpha_\downarrow) = (0, \pi)$.

III. TOPOLOGICAL PROPERTIES

A. Topological index

Topological quantum numbers are known to play an important role in characterizing the topological order phases. To compute the topological invariant that distinguishes these phases, we may consider our 2D superconductor model described by a Hamiltonian $H(\mathbf{k})$ in momentum space. By diagonalize $H(\mathbf{k})|\psi_n(\mathbf{k})\rangle = \varepsilon_n(\mathbf{k})|\psi_n(\mathbf{k})\rangle$, we can obtain a collection of bands $\varepsilon_n(\mathbf{k})$ and eigenstates $\psi_n(\mathbf{k})$ for integer n . The Chern number assigned to the n -th band based on Berry connection is defined by

$$C_n = \frac{i}{2\pi} \int d^2\mathbf{k} [\partial_{k_x} \langle \psi_n | \partial_{k_y} \psi_n \rangle - \partial_{k_y} \langle \psi_n | \partial_{k_x} \psi_n \rangle] \quad (11)$$

B. Entanglement spectrum

Besides of the Chern number, a topological phase can be also characterized by the quantum entanglement between the subsystem and the environment [50–55]. Given a ground state wave function $|\Psi\rangle$, one can calculate the reduced density matrix, ρ_A , for a subsystem A by tracing over the environment. The eigenvalues λ_α of the reduced density matrix is so-called “entanglement spectrum” [52], which carries nonlocal information and has been applied for calculating Berry phase and zero-energy edge states [56]. For example, the degeneracy of the entanglement spectrum has recently been implemented to

characterize the topological orders for some 2D quantum Hall states and for some 1D SPT phases [52].

For 1D Kitaev model, λ_α is given by the eigenvalues of the block Green’s function matrix, i.e., $G_{i,j} \equiv \langle c_i c_j^\dagger \rangle$ with the site indices i and j inside the subsystem A . In Ref. [56–58], it has been shown that the zero energy mode of the 1D Kitaev model corresponds to the degeneracy of $\lambda_\alpha = 1/2$ in the entanglement spectrum, i.e. the pair of zero modes at the two ends of Kitaev’s chain contribute the maximal entanglement between the subsystem A and environment. Besides of entanglement spectrum, a topological phase transition can be also identified by the entanglement entropy of the subsystem (given by $S_A = -Tr \rho_A \log \rho_A$) after tracing out the environment.

It has been known that the entanglement spectrum λ_α of the subsystem A can be obtained by diagonalizing the entire Green’s function matrix $G_{\mathbf{r}_1, \sigma_1, \mathbf{r}_2, \sigma_2}$ [55–58], where (\mathbf{r}_1, σ_1) and (\mathbf{r}_2, σ_2) are restricted in the subsystem A . When a 2D translationally invariant system is considered, we can divide our system into two parts along x -direction, and keep y -direction translationally invariant by applying a periodic boundary condition. The resulting Hamiltonian is then block-diagonal in terms of the wave number k_y , i.e. $H = \sum_{k_y} H_{k_y}$, where H_{k_y} is a 1D Hamiltonian for each given k_y subspace. Similar calculation along y direction can be also obtained by applying periodic boundary condition in the x direction first.

After applying periodic boundary condition in one direction (say y) only, we could choose interface along the x -direction and the entire Green’s function matrix of wave number k_y is given by

$$G(k_y)_{x_1, \sigma_1, x_2, \sigma_2} = \frac{1}{L_x} \sum_{k_x, k_y \in BZ} e^{ik_x(x_1 - x_2)} G(k_x, k_y)_{\sigma_1, \sigma_2}, \quad (12)$$

where L_x is the number sites in the x -direction and k_x, k_y takes values in the first Brillouin zone. $G(k_x, k_y)_{\sigma_1, \sigma_2}$ is a 4×4 matrix determined by the eigenvectors of mean-field Hamiltonian Eq. 4. We numerically diagonalize the block’s Green’s function for the subsystem A with a finite size, e.g., $L_A = 20$ and $L = 40$ as shown in Fig. 1 (b). The numerical results converges and is independent of the choices of subsystem in the thermal dynamic limit, $L \gg L_A \gg 1$.

C. Topological edge mode

Besides the calculation of entanglement spectrum of a bulk, we also investigate the edge state properties for the bilayer system numerically. According to the bulk-edge correspondence, a nontrivial bulk topological phase should imply the existence of edge states inside the gap. In order to study these edge states more clearly in the 2D systems, we first do Fourier transform along a direction parallel to the edge to get a family of 1D Hamiltonians, which are parametrized by the wave number along the edge. More precisely, for example, we can make Fourier transform along the y -direction first for the field operator, $c_{x,y,\sigma} = \frac{1}{\sqrt{L_y}} \sum_{k_y} e^{iyk_y} c_{x,k_y,\sigma}$ with L_y being the lattice size along the y direction (periodic boundary

condition). An effective BdG Hamiltonian can then be easily derived to be $H_{\text{BdG}} = \sum_{k_y} H_{k_y}$, where

$$H_{k_y} = \sum_{x,\sigma=\uparrow,\downarrow} \left[(-\mu - 2t \cos k_y) c_{x,k_y,\sigma}^\dagger c_{x,k_y,\sigma} \right. \quad (13)$$

$$\left. - t c_{x,k_y,\sigma}^\dagger c_{x+1,k_y,\sigma} + e^{i\phi_\sigma} \Delta_p c_{x,k_y,\sigma}^\dagger c_{x+1,-k_y,\sigma} \right.$$

$$\left. + i e^{i\alpha_\sigma} e^{i\phi_\sigma} \Delta_p e^{ik_y} c_{x,k_y,\sigma}^\dagger c_{x,-k_y,\sigma} + h.c. \right]$$

$$+ \sum_x \left[-t_z c_{x,k_y,\uparrow}^\dagger c_{x,k_y,\downarrow} + \Delta_s c_{x,k_y,\uparrow}^\dagger c_{x,-k_y,\downarrow} + h.c. \right]$$

One can see that

$$H_{k_y}^{4\text{-leg}} = H_{k_y} + H_{-k_y} \quad (14)$$

is a four-leg ladder system for a given momentum k_y . We could then apply a finite size exact diagonalization in the x -direction, making the original 2D system mapped to an effective 1D 4-leg ladder system. Since the system has two boundary edges at $x = 1$ and $x = L_x$, we could then solve the eigenmode spectrum of this finite size system as a function of the momentum k_y numerically.

IV. RESULTS FOR TWO EXAMPLES

In general, a phase transition between different phases occur only when the energy gap of the bulk spectrum closes. Thus, to identify parameter regions for which different (topological phases) are realized, we would first examine the bulk spectrum of the system. To obtain the bulk spectrum, we would adopt periodic boundary condition (PBC) to form bulk Hamiltonian and study the phase boundary. On the other hand, from the bulk-edge correspondence, a nontrivial bulk topological number implies the existence of gapless edge states. To investigate edge states, we would consider the open boundary condition along one direction to form a family of 1D Hamiltonians parametrized by wave number k . For example, by solving numerically the energy spectrum as a function of the momentum k_y in the y direction, we could study edge states near the interface. By tuning parameters of the Hamiltonian, the phase transition will occur. We may classify these phases into two types according to their energy gap of the bulk spectrum and topological order: Type I: topological order phase with symmetry \mathcal{P} by fixed $t_z \neq 0$ and $(\phi_\uparrow, \phi_\downarrow) = (0, \pi)$, $(\alpha_\uparrow, \alpha_\downarrow) = (0, \pi)$. Type II: topological order phase with symmetries, $\mathcal{P}, \mathcal{T}, \mathcal{C}$ by fixed $t_z = 0$ and $(\phi_\uparrow, \phi_\downarrow) = (0, 0)$, $(\alpha_\uparrow, \alpha_\downarrow) = (0, \pi)$

A. Type I: $(\phi_\uparrow, \phi_\downarrow, \alpha_\uparrow, \alpha_\downarrow) = (0, \pi, 0, \pi)$.

As a check and benchmark, we first calculate the the energy eigenvalues of the bulk Hamiltonian for such a anti-symmetric case with $(\phi_\uparrow, \phi_\downarrow) = (0, \pi)$ and $(\alpha_\uparrow, \alpha_\downarrow) = (0, \pi)$. As explained above, depending on the parameter t_z/t and $|\Delta_s|/t$, the corresponding phase will make a transition to either topological order phase or trivial phase. In the following, we

would show the details for energy spectra and entanglement spectra. A simple evaluation shows that the eigenvalues of matrix in Eq. (4) with $(\phi_\uparrow, \phi_\downarrow) = (0, \pi)$ and $(\alpha_\uparrow, \alpha_\downarrow) = (0, \pi)$ are simply $\pm E_{\mathbf{k}}$, where the energy dispersion for this system are

$$E_{\mathbf{k}} = \pm \left[\varepsilon_{\mathbf{k}}^2 + t_z^2 + 4|\Delta_p|^2 (\sin^2 k_x + \sin^2 k_y) + |\Delta_s|^2 \right. \\ \left. \pm 2|t_z| \sqrt{\varepsilon_{\mathbf{k}}^2 + |\Delta_s|^2 + 4|\Delta_p|^2 \sin^2 k_x} \right]^{1/2}.$$

We discuss two cases: $|\Delta_s|/t = 0$ (see Fig. 2(a)) and $|\Delta_s|/t = 1$ (see Fig. 2(b)). The phase diagram can be obtained from computing the number $N_{1/2}$ of the $\lambda_\alpha = 1/2$ modes in entanglement spectrum from the Green's function matrix. In our case, we numerically diagonalize the Green's function for subsystem A with a finite size, e.g. $L_y = 20$ of full lattice size 40×40 . When there is an extensive number of the $\lambda_\alpha = 1/2$ mode, it indicates an extensive number of the entangling boundary modes localized at the interface between subsystem A and subsystem B . These entanglement boundary modes mimic the dispersionless boundary modes of the gapless topological phases, such as the flat bands on the zigzag edge of graphene [55]. As shown in Figs. 2 (a)(b), the "large" number $N_{1/2}$ indicates the gapless region and the phase boundaries between the gapped and the gapless regions can be shown from the intensity plot.

In this model, the gap of the system for $|\Delta_s|/t = 0$ closes only when the following condition is satisfied:

$$4|\Delta_p|^2 \sin^2 k_y = \left(\sqrt{\varepsilon_{\mathbf{k}}^2 + 4|\Delta_p|^2 \sin^2 k_x} \pm t_z \right)^2 = 0. \quad (15)$$

Therefore, the gap closes at $k_y = 0$ or $k_y = \pi$. From a straightforward calculation, it is found that this condition is equivalent to $(-\mu/t \mp 2)^2 + 4 - 2(-\mu/t \mp 2) \cos k_x = (t_z/t)^2$, where “-” term corresponds to $k_y = 0$, “+” term corresponds to $k_y = \pi$, and k_x is related to the lattice size. This is, the gap of the system closes at \mathbf{k} which is determined by Hamiltonian parameters.

First, we consider the parameters with $|\Delta_s|/t = 0$ and $t_z/t = 0$, then the Hamiltonian reduces to a bilayer chiral p-wave superconductor without interlayer interaction. It can be reduced to 2d chiral p-wave superconductor model. There are three phases separated by three quantum critical points at $\mu/t = 0, \pm 4$, which are labeled by the Chern number (Ch) as $\text{Ch} = 0$ ($|\mu/t| > 4$), $\text{Ch} = -1$ ($-4 < \mu/t < 0$), and $\text{Ch} = 1$ ($0 < \mu/t < 4$). Since in the torus geometry, there are two entangling boundaries that will lead to an additional twofold degeneracy together with the twofold degeneracy from the bilayer of the system in the entanglement spectrum. The number of the $\lambda_\alpha = 1/2$ in the entanglement spectrum is four times the Chern number, $N_{1/2} = 4|\text{Ch}|$. I.e, $N_{1/2} = 4$ when the Chern number is unity ($\text{Ch} = \pm 1$). Our numerical results agree with the analytic result of the Chern number, confirming the topological properties in our current system. There are two phases which are labeled by $N_{1/2}$ as $N_{1/2} = 4$ (topological phase) and $N_{1/2} = 0$ (trivial phase).

We shall now look more carefully into the edge states. We impose the periodic boundary condition in the x direction.

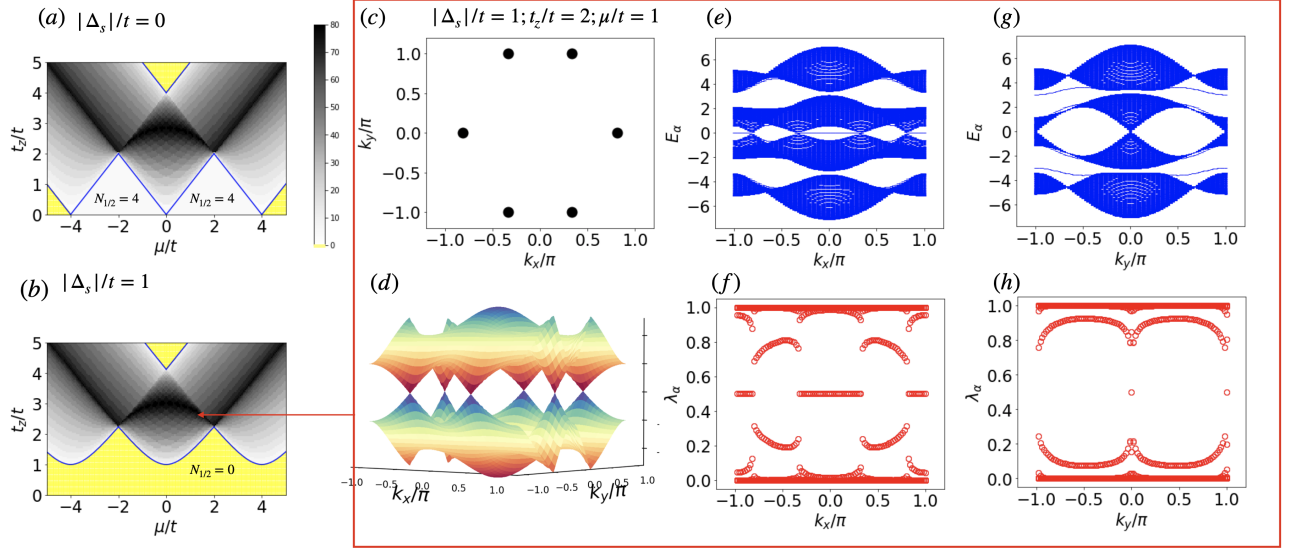


FIG. 2. The numerical results $N_{1/2}$ of Hamiltonian Eq. (4) for $(\alpha_\uparrow, \alpha_\downarrow) = (0, \pi)$ and $(\phi_\uparrow, \phi_\downarrow) = (0, \pi)$ with (a) $|\Delta_s|/t = 0$, (b) $|\Delta_s|/t = 1$. $N_{1/2}$ is the number of the degenerate entanglement spectrum at $\lambda_\alpha = 1/2$ with lattice size 40×40 and cut system along x-direction. In particular, the result of $N_{1/2} = 0$ is marked in yellow. The blue line shows the boundary between gapped and gapless state, which is determined by energy spectra. And, the gapless states with finite $N_{1/2}$ is in grey region. (c) (d) The bulk gap closes at particular momentum k_x^* and k_y^* for $\mu/t = 1$, $|\Delta_s|/t = 1$, and $t_z/t = 2$ with finite size $L = 100$. (e) The energy spectra as a function of k_x (the momentum in x direction), $k_x \in (-\pi, \pi]$ with finite size $L = 100$ with boundaries at $y = 1$ and $y = 100$ for $|\Delta_s|/t = 1$, $t_z/t = 2$ and $\mu/t = 1$. (f) The corresponding spectra of the reduced density with cut at $y = 1$ and $y = 50$. (g) The energy spectra and (h) the entanglement spectra as a function of k_y .

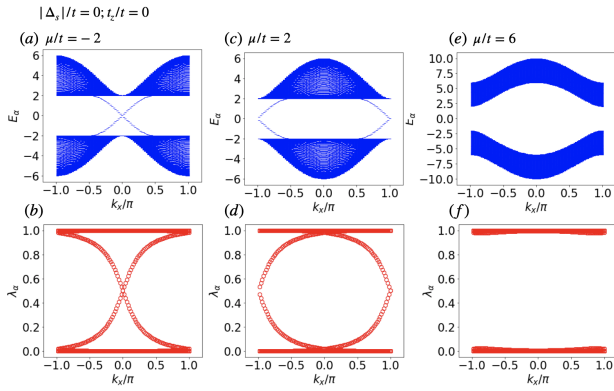


FIG. 3. The energy spectra and the corresponding entanglement spectra as a function k_x with finite size $L = 100$ for $(\phi_\uparrow, \phi_\downarrow) = (0, \pi)$, $(\alpha_\uparrow, \alpha_\downarrow) = (0, \pi)$, $t_z/t = 0$ and $|\Delta_s|/t = 0$ with (a)(b) $\mu/t = -2$, (c)(d) $\mu/t = 2$, and (e)(f) $\mu/t = 6$.

Fourier transforming along the x direction and obtain a family of 1D Hamiltonians parametrized by k_x . Suppose that the system has two edges at $y = 1$ and $y = L$. By solving numerically the energy spectrum as a function of the momentum k_x in the y direction, we then study edge states. Figs. 3(a)(c)(e) show the energy spectra with open boundaries along y axis and translational invariance along the x direction. It shows zero energy modes appear for $k_x = 0$ or $k_x = \pi$. On the other hand, the entanglement spectrum can mimic the physical edge spectrum for the torus geometry. The correspond-

ing edge modes in the entanglement spectrum will be localized at the entangling boundary between the subsystem A and the subsystem B , and the entanglement spectra are shown in Figs. 3 (b)(d)(f). These results are consistent with the bulk-edge correspondence again. The Figs 3(a)(c) show that these points are topological phase with $N_{1/2} = 4$. In $\mu/t = 2$, the fourfold degeneracy occur at $k_x = 0$. In $\mu/t = -2$, the fourfold degeneracy occur at $k_x = \pi$. The $N_{1/2}$'s appear at different k_x corresponding to the different topological phases.

Next, we consider the case $|\Delta_s|/t \neq 1$. In Fig. 2 (b), we find there exist a gapless phase in the phase diagram. The gap closing points (k_x^*, k_y^*) are determined by Eq. (15) with $|\Delta_s|/t = 1$, $|t_z|/t = 2$, $|\mu|/t = 1$ in Figs. 2(c)(d). We then impose the periodic boundary condition in the both x direction and y direction. The energy spectra with open boundary condition as a function of momentum are shown in Fig. 2(e)(g). The corresponding spectra of the reduced density with open ends also is shown in Fig. 2(f)(h). It shows zero energy modes appear between the four gapless points k_x^* . These results are consistent with the bulk-edge correspondence for the topological gapless phases [59].

B. Type II: $(\phi_\uparrow, \phi_\downarrow, \alpha_\uparrow, \alpha_\downarrow) = (0, 0, 0, \pi)$.

We consider the fixed parameters with $(\phi_\uparrow, \phi_\downarrow) = (0, 0)$, $(\alpha_\uparrow, \alpha_\downarrow) = (0, \pi)$ at $t_z/t = 0$. In this case, the mean-field Hamiltonian has parity and time reversal symmetry. In particular, this model can be transformed to Kondo lattice

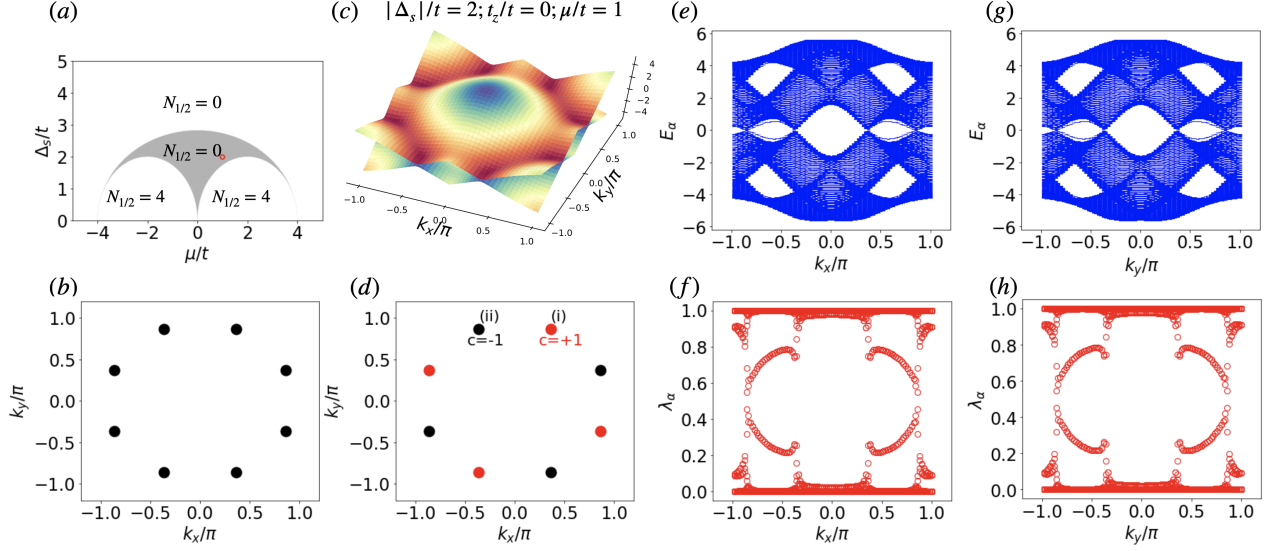


FIG. 4. (a) The phase diagram as computed via the energy eigenvalue for $t_z/t = 0$, $\phi_\uparrow = \phi_\downarrow = 0$ and $\alpha_\uparrow = 0$, $\alpha_\downarrow = \pi$ with under periodic boundary condition. Shaded regimes are gapless phases. For $\mu/t = 1$, $|\Delta_s|/t = 2$, and $t_z/t = 0$, (b) The bulk gap closes at particular momentum k_x^* and k_y^* (belong to C_{4v} group) with finite size $L = 100$. (c) The lower energy spectra and (d) topological charge of the function of momentum k_x and k_y . The energy spectra as a function (e) k_x and (g) k_y with finite size $L = 100$ and the corresponding entanglement spectra as a function of (f) k_x and (h) k_y .

model in some special case [1], which has the time-reversal symmetry and rotation symmetry. In Ref [1], they studied a topological transition from a strong topological insulator to a weak topological insulator in a three-dimensional Kondo lattice. They showed the transitions between two topological phases must go through gapless phases. In this section, we would show the similar phase transition in the bilayer system.

First, it is easy to check that for such a anti-symmetric case with fixed $t_z/t = 0$, the energy dispersion for this system are

$$E_{\mathbf{k}} = \pm \left[\varepsilon_{\mathbf{k}}^2 + \left(|\Delta_s| \pm 2|\Delta_p| \sqrt{\sin^2 k_x + \sin^2 k_y} \right)^2 \right]^{1/2}$$

as expected. Again, the energy gap of the system closes only when the following condition is satisfied:

$$\varepsilon_{\mathbf{k}}^2 = \left(|\Delta_s| \pm 2|\Delta_p| \sqrt{\sin^2 k_x + \sin^2 k_y} \right)^2 = 0.$$

It is found that this condition is equivalent to

$$\begin{aligned} \cos^2 k_x + \cos^2 k_y &= 2 - |\Delta_s|^2/4t^2, \\ \cos k_x + \cos k_y &= -\mu/2t. \end{aligned} \quad (16)$$

The gap closing points are shown in Fig. 4(a). It is obvious to see that if $\mathbf{k} = (k_x, k_y)$ is a generic solution, $(\pm k_x, \pm k_y)$ and $(\pm k_y, \pm k_x)$ are also solutions, i.e. there are eight-fold degeneracy, belong to C_{4v} group (see Fig. 4(b)). In Fig. 4(c), we show the case with $\mu/t = 1$, $|\Delta_s|/t = 2$, and $t_z/t = 0$ numerically. On the other hand, we also calculate the entanglement spectrum and we find that there are regions with a large number of $N_{1/2}$ in the entanglement spectrum. These regions are the gapless phases which is same as the previous analysis.

However, in this case, we do not find the Majorana zero modes at each end in gapless region (see Figs. 4(e)(g)) for the open boundary conditions in both x and y directions. For the entanglement spectrum, we also do not find any entangling boundary modes with $\lambda_\alpha = 1/2$. The absence of Majorana edge modes does not indicate it is a trivial gapless phase. Duo to the perfect cancellation of the topological charges of the gapless points in the bulk projected on the boundary, the Majorana zero modes are gapped out.

Nevertheless, we can directly calculate the topological charge which is given by the winding number that corresponds to eigenstate of effective Hamiltonian of a gapless point. To compute the effective Hamiltonian, We first expand the Hamiltonian around the gapless points (k_x^0, k_y^0) up to linear terms, i.e. $\mathbf{k} = \mathbf{k}^0 + \mathbf{q}$, so that $H(\mathbf{k}) \sim H_0(\mathbf{k}^0) + H_1(\mathbf{q})$, where

$$\begin{aligned} H_0(\mathbf{k}^0) &= \varepsilon_{\mathbf{k}} (\sigma_3 \otimes \sigma_0) - \Delta_s (\sigma_2 \otimes \sigma_2) \\ &\quad - 2\Delta_p [\sin(k_x^0)] (\sigma_2 \otimes \sigma_0) - 2\Delta_p [\sin(k_y^0)] (\sigma_1 \otimes \sigma_3) \end{aligned}$$

and

$$\begin{aligned} H_1(\mathbf{q}) &= 2t[q_x \sin(k_x^0) + q_y \sin(k_y^0)] (\sigma_3 \otimes \sigma_0) \\ &\quad - 2\Delta_p q_x \cos(k_x^0) (\sigma_2 \otimes \sigma_0) - 2\Delta_p q_y \cos(k_y^0) (\sigma_1 \otimes \sigma_3). \end{aligned}$$

Since the analytic solutions of H_0 are not generally available, we first numerically calculate its two eigenvectors, $|v_1\rangle$ and $|v_2\rangle$, with zero eigenenergy at $E_k = \pm 0$. Here, we just consider gapless points (see Fig. 4(b)) at $(\alpha_\uparrow, \alpha_\downarrow) = (0, \pi)$, $(\phi_\uparrow, \phi_\downarrow) = (0, 0)$, $\mu/t = 1$, $|\Delta_s|/t = 2$, and $t_z/t = 0$. The effective Hamiltonian near the gapless points is then obtained by projecting the leading order Hamiltonian, $H_1(\mathbf{q})$, onto the

subspace of $\{|v_1\rangle, |v_2\rangle\}$, i.e.

$$H_{\text{eff}}(\mathbf{q}) = \begin{pmatrix} \langle v_1 | H_1(\mathbf{q}) | v_1 \rangle & \langle v_1 | H_1(\mathbf{q}) | v_2 \rangle \\ \langle v_2 | H_1(\mathbf{q}) | v_1 \rangle & \langle v_2 | H_1(\mathbf{q}) | v_2 \rangle \end{pmatrix} \\ = v_x(\mathbf{k}^0)q_x\sigma'_x + v_y(\mathbf{k}^0)q_y\sigma'_y, \quad (17)$$

Here $v_x(\mathbf{k}^0)$ and $v_y(\mathbf{k}^0)$ are two "velocity functions" of the gapless point. Note that $\sigma'_{x/y}$ are Pauli matrix expressed in another basis, which are rotated from $\{|v_1\rangle, |v_2\rangle\}$, in order to simplify the notation to the conventional Weyl point form in the 2D system.

Note that, within this new basis, the chiral symmetry is given by σ'_z , i.e. $\sigma'_z H_{\text{eff}}(\mathbf{q}) \sigma'_z = -H_{\text{eff}}(\mathbf{q})$. As a result, we can further rescale the effective Hamiltonian and express it into polar coordinate:

$$H_{\text{eff}}(\mathbf{q}) = E_1(\mathbf{q}) \begin{pmatrix} 0 & e^{i\theta_{\mathbf{q}}} \\ e^{-i\theta_{\mathbf{q}}} & 0 \end{pmatrix}, \quad (18)$$

where $E_1(\mathbf{q}) \equiv \sqrt{v_x(\mathbf{k}^0)^2 q_x^2 + v_y(\mathbf{k}^0)^2 q_y^2}$ and $\theta_{\mathbf{q}} \equiv \tan^{-1} \left[\frac{v_y(\mathbf{k}^0)q_y}{v_x(\mathbf{k}^0)q_x} \right]$. The corresponding winding number could then be calculated to be

$$W = \frac{1}{2\pi i} \oint d\theta_{\mathbf{q}} \partial_{\theta_{\mathbf{q}}} e^{i\theta_{\mathbf{q}}} = 1. \quad (19)$$

The topological charge of the gapless points at point (ii) (see Fig. 4(d)) is $W = -1$, since one of velocity function ($v_x(\mathbf{k}^0)$ and $v_y(\mathbf{k}^0)$) changes its sign in Eq. (17). Following similar approach, we can get all gapless points's topological charge shown in the Fig. 4(d).

V. EVIDENCE IN TIME-OF-FLIGHT EXPERIMENT

In the literature, there have been several proposals to measure Majorana modes. In condensed matter systems, the chiral Majorana fermions in two dimensions can be measured from the quantized thermal Hall conductivity [60–62] or from the scanning tunneling microscopy [63–67]. In cold-atom experiments, an alternative detection of the Majorana modes is from the long-distance Majorana correlation from the time-of-flight (ToF) experiments [68].

However, in the gapless topological superfluid proposed here, the Majorana zero modes appear when the relative gauge phases between the inter-layer s -wave pairing and the intra-layer p -wave pairing order parameters are changed from their conventional value, $(\alpha_{\uparrow}, \alpha_{\downarrow}, \phi_{\uparrow}, \phi_{\downarrow}) = (0, 0, 0, 0)$. According to Table I, the most generic Majorana modes should appear at Type I, where $t_z \neq 0$ and $(\alpha_{\uparrow}, \alpha_{\downarrow}, \phi_{\uparrow}, \phi_{\downarrow}) = (0, \pi, 0, \pi)$.

Since such kind of many-body gauge phase may not be easily manipulated, it becomes important to how to measure such spontaneously emergent gauge phase in the present experiment. According to the calculated positions of the associated gapless points, see Fig. 2 Type I case, the low energy spectrum are highly asymmetric in the k_x and k_y direction due to

the "six-fold" gapless point structure shown in (c). It is therefore interesting if one could observe this in the simple ToF experiment too.

It is known that the time-of-flight image for a free expansion time t is obtained by integrating over the z direction, i.e.,

$$n_{\text{ToF}}(x, y) \propto \int_{-\infty}^{\infty} dz n_{m\mathbf{r}/\hbar t} \left| \tilde{w}_0 \left(\frac{m\mathbf{r}}{\hbar t} \right) \right|^2 \quad (20)$$

where $\tilde{w}_0(m\mathbf{r}/\hbar t)$ is the lowest band Wannier function of the optical lattice in momentum space. The final position $\mathbf{r} = \hbar\mathbf{k}t/m$ is to be transformed into the initial momentum under the assumption of long time-of-flight and free expansion. $n_{\mathbf{k}}$ is the momentum distribution *inside* before expansion,

$$n_{\mathbf{k}} = \sum_{\mathbf{j}, \mathbf{j}'} \sum_{\sigma, \sigma'} \langle G | c_{\mathbf{j}, \sigma}^{\dagger} c_{\mathbf{j}', \sigma} | G \rangle e^{i(j_x - j'_x)k_x a} e^{i(j_y - j'_y)k_y a} \\ \times e^{i(\sigma - \sigma')k_z d} \quad (21)$$

where $|G\rangle$ is the ground-state wave function obtained by diagonalizing the mean-field Hamiltonian. $\mathbf{j} = (j_x, j_y)$ is the lattice index in the 2D plane and $\sigma = \pm 1/2$ for layer index.

In Fig. 5, we show the TOF images for the system with $t_z/t = 2$, $\mu/t = 0$, and $|\Delta_s|/t = 1$ in a bilayer system of $L_x = L_y = 100$ (open boundary condition). Results obtained by both $(\alpha_{\uparrow}, \alpha_{\downarrow}, \phi_{\uparrow}, \phi_{\downarrow}) = (0, 0, 0, 0)$ and $(\alpha_{\uparrow}, \alpha_{\downarrow}, \phi_{\uparrow}, \phi_{\downarrow}) = (0, \pi, 0, \pi)$ are shown together in (a1) and (a2) respectively. These ToF images are taken by integrating along the z axis (perpendicular to the layer) after long time of flight. One could see that is a deep valley at certain finite value in the y axis.

In order to investigate results of these two different gauge phases more specifically, in (b1) and (b2) we further show their integrated density distribution both in the x and y directions for comparison. We could see that in the regime of gapless topological phase (b2) (same as the case in Fig. 2), the ToF images show a significant difference in the x and y directions, while no such difference in the conventional phases shown in (b1). The most significant difference in their distribution appears at $k_y a = \pm\pi$, or equivalently at $y = \pm\pi\hbar t/ma$. This is obvious due to the position of double gapless Weyl points at $k_y = \pm\pi/a$ as shown in Fig. 2(c). It is because at 2D system, the presence of gapless points makes the density of states almost zero in the low energy regime, while no such a similar situation in the k_x direction. On the other hand, when considering the system with the conventional gauge phase in (a1) and (b1), the system is a gaped phase and therefore not much difference in the x and y directions. Therefore, our results show that the phase modulation of the gapless topological superfluid could also be observed easily by analyzing the ToF images.

VI. CONCLUSION

In this paper, we propose that a topological state can be prepared and observed in a paired 2D p -wave superfluids, where spin polarized fermionic atoms are loaded in a bilayer optical lattice with a weak coupling to Rydberg excited states The

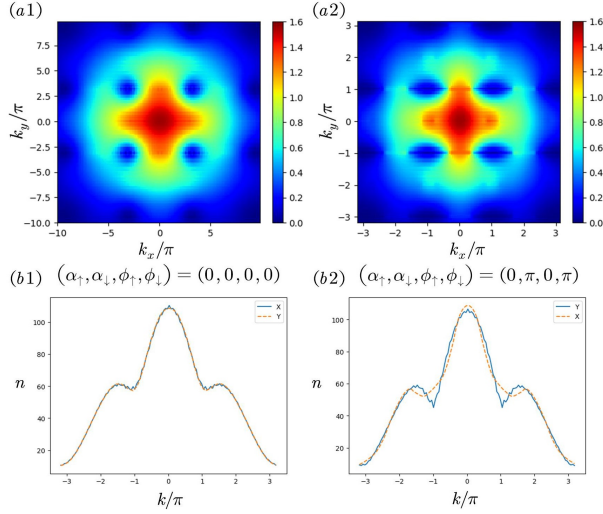


FIG. 5. (a1) and (a2) are the calculated ToF images for two different gauge phases, $(\alpha_\uparrow, \alpha_\downarrow, \phi_\uparrow, \phi_\downarrow) = (0, 0, 0, 0)$ and $(\alpha_\uparrow, \alpha_\downarrow, \phi_\uparrow, \phi_\downarrow) = (0, \pi, 0, \pi)$. (b1) and (b2) are the integrated density distribution, $n_{ToF}(x, y)$, for (a1) and (a2) respectively. Both direction in x and y direction are shown together for comparison.

associated quantum degenerate Majorana zero modes appear in the edge, confirmed by the zero energy mode and entanglement spectrum numerics. Our work paves the way for future investigation of the many-body physics with non-Abelian statistics under time-reversal symmetry.

ACKNOWLEDGMENTS

We thank useful discussion with Chung-Hou Chung, Yi-Ping Huang, Chung-Yu Mou, and Jih-Shih You. CYH is supported by the MOST of Taiwan under Grants No. 108-2112-M-029 -006 -MY3. DWW is supported by National Center for theoretical Sciences and by the Higher Education Sprout Project funded by the Ministry of Science and Technology and Ministry of Education in Taiwan.

Appendix A: The single-particle energy spectra of mean-field Hamiltonian

In this appendix, we shall summarize the single-particle energy spectra of mean-field Hamiltonian $H(\mathbf{k})$. First we fix $\alpha_\uparrow = \alpha_\downarrow = 0$ and shown in Table III. In particular, we can find the spectra of $\phi_\uparrow = \phi_\downarrow = 0$ and $\phi_\uparrow = \phi_\downarrow = \pi/2$ up to a 90 degree rotation transformation. This is, once we replace k_x to k_y , these two spectra are the same.

$\phi_\uparrow = \phi_\downarrow = 0$	$E_{\mathbf{k}} = \pm \left[\varepsilon_{\mathbf{k}}^2 + t_z^2 + 4 \Delta_p ^2 (\sin^2 k_x + \sin^2 k_y) + \Delta_s ^2 \pm 2\sqrt{\varepsilon_{\mathbf{k}}^2 t_z^2 + t_z^2 \Delta_s ^2 + 4 \Delta_p ^2 \Delta_s ^2 \sin^2 k_x} \right]^{1/2}$
$\phi_\uparrow = \phi_\downarrow = \pi/2$	$E_{\mathbf{k}} = \pm \left[\varepsilon_{\mathbf{k}}^2 + t_z^2 + 4 \Delta_p ^2 (\sin^2 k_x + \sin^2 k_y) + \Delta_s ^2 \pm 2\sqrt{\varepsilon_{\mathbf{k}}^2 t_z^2 + t_z^2 \Delta_s ^2 + 4 \Delta_p ^2 \Delta_s ^2 \sin^2 k_y} \right]^{1/2}$
$\phi_\uparrow = 0, \phi_\downarrow = \pi$	$E_{\mathbf{k}} = t_z \pm \left[\varepsilon_{\mathbf{k}}^2 + 4 \Delta_p ^2 (\sin^2 k_x + \sin^2 k_y) - 4 \Delta_p \Delta_s \sin k_y + \Delta_s ^2 \right]^{1/2}$ $E_{\mathbf{k}} = -t_z \pm \left[\varepsilon_{\mathbf{k}}^2 + 4 \Delta_p ^2 (\sin^2 k_x + \sin^2 k_y) + 4 \Delta_p \Delta_s \sin k_y + \Delta_s ^2 \right]^{1/2}$

TABLE II. The single-particle energy spectra of mean-field Hamiltonian with $\alpha_\uparrow = \alpha_\downarrow = 0$.

Then we consider $\alpha_\uparrow = 0, \alpha_\downarrow = \pi$ and shown in Table IV.

$\phi_\uparrow = \phi_\downarrow = \pi/2$	$E_{\mathbf{k}} = \pm \left[\varepsilon_{\mathbf{k}}^2 + t_z^2 + 4 \Delta_p ^2 (\sin^2 k_x + \sin^2 k_y) + \Delta_s ^2 \pm 2 t_z \sqrt{\varepsilon_{\mathbf{k}}^2 + \Delta_s ^2 + 4 \Delta_p ^2 \sin^2 k_y} \right]^{1/2}$
$\phi_\uparrow = 0, \phi_\downarrow = \pi$	$E_{\mathbf{k}} = \pm \left[\varepsilon_{\mathbf{k}}^2 + t_z^2 + 4 \Delta_p ^2 (\sin^2 k_x + \sin^2 k_y) + \Delta_s ^2 \pm 2 t_z \sqrt{\varepsilon_{\mathbf{k}}^2 + \Delta_s ^2 + 4 \Delta_p ^2 \sin^2 k_x} \right]^{1/2}$

TABLE III. The single-particle energy spectra of mean-field Hamiltonian with $\alpha_\uparrow = 0, \alpha_\downarrow = \pi$.

[1] P.-H. Chou, L.-J. Zhai, C.-H. Chung, C.-Y. Mou, and T.-K. Lee, Emergence of a fermionic finite-temperature critical point in a

kondo lattice, Phys. Rev. Lett. **116**, 177002 (2016).

- [2] E. Majorana, Teoria simmetrica dell'elettrone e del positrone, *Il Nuovo Cimento* (1924-1942) **14**, 171 (2008).
- [3] C.-K. Chiu, J. C. Y. Teo, A. P. Schnyder, and S. Ryu, Classification of topological quantum matter with symmetries, *Rev. Mod. Phys.* **88**, 035005 (2016).
- [4] M. Cheng, M. Zaletel, M. Barkeshli, A. Vishwanath, and P. Bonderson, Translational symmetry and microscopic constraints on symmetry-enriched topological phases: A view from the surface, *Phys. Rev. X* **6**, 041068 (2016).
- [5] A. Y. Kitaev, Unpaired majorana fermions in quantum wires, *Physics-Uspekhi* **44**, 131 (2001).
- [6] L. Fu and C. L. Kane, Superconducting proximity effect and majorana fermions at the surface of a topological insulator, *Phys. Rev. Lett.* **100**, 096407 (2008).
- [7] J. D. Sau, R. M. Lutchyn, S. Tewari, and S. Das Sarma, Generic new platform for topological quantum computation using semiconductor heterostructures, *Phys. Rev. Lett.* **104**, 040502 (2010).
- [8] J. Alicea, Majorana fermions in a tunable semiconductor device, *Phys. Rev. B* **81**, 125318 (2010).
- [9] M. Sato, Y. Takahashi, and S. Fujimoto, Non-abelian topological orders and majorana fermions in spin-singlet superconductors, *Phys. Rev. B* **82**, 134521 (2010).
- [10] R. M. Lutchyn, J. D. Sau, and S. Das Sarma, Majorana fermions and a topological phase transition in semiconductor-superconductor heterostructures, *Phys. Rev. Lett.* **105**, 077001 (2010).
- [11] V. Mourik, K. Zuo, S. M. Frolov, S. R. Plissard, E. P. A. M. Bakkers, and L. P. Kouwenhoven, Signatures of majorana fermions in hybrid superconductor-semiconductor nanowire devices, *Science* **336**, 1003 (2012).
- [12] A. Das, Y. Ronen, Y. Most, Y. Oreg, M. Heiblum, and H. Shtrikman, Zero-bias peaks and splitting in an al-inas nanowire topological superconductor as a signature of majorana fermions, *Nature Physics* **8**, 887 (2012).
- [13] L. P. Rokhinson, X. Liu, and J. K. Furdyna, The fractional a.c. josephson effect in a semiconductor-superconductor nanowire as signature of majorana particles, *Nature Physics* **8**, 795 (2012).
- [14] M. T. Deng, C. L. Yu, G. Y. Huang, M. Larsson, P. Caroff, and H. Q. Xu, Anomalous zero-bias conductance peak in a nb-insb nanowire-nb hybrid device, *Nano Letters* **12**, 6414 (2012).
- [15] S. Tewari, S. Das Sarma, C. Nayak, C. Zhang, and P. Zoller, Quantum computation using vortices and majorana zero modes of a $p_x + ip_y$ superfluid of fermionic cold atoms, *Phys. Rev. Lett.* **98**, 010506 (2007).
- [16] Z. Shermadini, A. Krzton-Maziopa, M. Bendele, R. Khasanov, H. Luetkens, K. Conder, E. Pomjakushina, S. Weyeneth, V. Pomjakushin, O. Bossen, and A. Amato, Coexistence of magnetism and superconductivity in the iron-based compound $\text{Cs}_{0.8}(\text{fese}_{0.98})_2$, *Phys. Rev. Lett.* **106**, 117602 (2011).
- [17] X.-J. Liu, K. T. Law, and T. K. Ng, Realization of 2d spin-orbit interaction and exotic topological orders in cold atoms, *Phys. Rev. Lett.* **112**, 086401 (2014).
- [18] M. Sato, Y. Takahashi, and S. Fujimoto, Non-abelian topological order in s -wave superfluids of ultracold fermionic atoms, *Phys. Rev. Lett.* **103**, 020401 (2009).
- [19] R. Wakatsuki, M. Ezawa, and N. Nagaosa, Majorana fermions and multiple topological phase transition in kitaev ladder topological superconductors, *Phys. Rev. B* **89**, 174514 (2014).
- [20] R. Wakatsuki, M. Ezawa, Y. Tanaka, and N. Nagaosa, Fermion fractionalization to majorana fermions in a dimerized kitaev superconductor, *Phys. Rev. B* **90**, 014505 (2014).
- [21] A. Alecce and L. Dell'Anna, Extended kitaev chain with longer-range hopping and pairing, *Phys. Rev. B* **95**, 195160 (2017).
- [22] D. Vodola, L. Lepori, E. Ercolessi, A. V. Gorshkov, and G. Pupillo, Kitaev chains with long-range pairing, *Phys. Rev. Lett.* **113**, 156402 (2014).
- [23] Y. O. Dudin and A. Kuzmich, Strongly interacting rydberg excitations of a cold atomic gas, *Science* **336**, 887 (2012).
- [24] U. Raitzsch, V. Bendkowsky, R. Heidemann, B. Butscher, R. Löw, and T. Pfau, Echo experiments in a strongly interacting rydberg gas, *Phys. Rev. Lett.* **100**, 013002 (2008).
- [25] J. D. Pritchard, D. Maxwell, A. Gauguet, K. J. Weatherill, M. P. A. Jones, and C. S. Adams, Cooperative atom-light interaction in a blockaded rydberg ensemble, *Phys. Rev. Lett.* **105**, 193603 (2010).
- [26] J. Nipper, J. B. Balewski, A. T. Krupp, B. Butscher, R. Löw, and T. Pfau, Highly resolved measurements of stark-tuned Förster resonances between rydberg atoms, *Phys. Rev. Lett.* **108**, 113001 (2012).
- [27] P. Schauß, M. Cheneau, M. Endres, T. Fukuhara, S. Hild, A. Omran, T. Pohl, C. Gross, S. Kuhr, and I. Bloch, Observation of spatially ordered structures in a two-dimensional rydberg gas, *Nature* **491**, 87 (2012).
- [28] D. Jaksch, J. I. Cirac, P. Zoller, S. L. Rolston, R. Côté, and M. D. Lukin, Fast quantum gates for neutral atoms, *Phys. Rev. Lett.* **85**, 2208 (2000).
- [29] M. D. Lukin, M. Fleischhauer, R. Cote, L. M. Duan, D. Jaksch, J. I. Cirac, and P. Zoller, Dipole blockade and quantum information processing in mesoscopic atomic ensembles, *Phys. Rev. Lett.* **87**, 037901 (2001).
- [30] E. Urban, T. A. Johnson, T. Henage, L. Isenhower, D. D. Yavuz, T. G. Walker, and M. Saffman, Observation of rydberg blockade between two atoms, *Nature Physics* **5**, 110 (2009).
- [31] A. Gaëtan, Y. Miroshnychenko, T. Wilk, A. Chotia, M. Viteau, D. Comparat, P. Pillet, A. Browaeys, and P. Grangier, Observation of collective excitation of two individual atoms in the rydberg blockade regime, *Nature Physics* **5**, 115 (2009).
- [32] N. Henkel, R. Nath, and T. Pohl, Three-dimensional roton excitations and supersolid formation in rydberg-excited bose-einstein condensates, *Phys. Rev. Lett.* **104**, 195302 (2010).
- [33] N. Henkel, F. Cinti, P. Jain, G. Pupillo, and T. Pohl, Supersolid vortex crystals in rydberg-dressed bose-einstein condensates, *Phys. Rev. Lett.* **108**, 265301 (2012).
- [34] J. B. Balewski, A. T. Krupp, A. Gaj, S. Hofferberth, R. Löw, and T. Pfau, Rydberg dressing: understanding of collective many-body effects and implications for experiments, *New Journal of Physics* **16**, 063012 (2014).
- [35] H. P. Büchler, E. Demler, M. Lukin, A. Micheli, N. Prokof'ev, G. Pupillo, and P. Zoller, Strongly correlated 2d quantum phases with cold polar molecules: Controlling the shape of the interaction potential, *Phys. Rev. Lett.* **98**, 060404 (2007).
- [36] F. Cinti, P. Jain, M. Boninsegni, A. Micheli, P. Zoller, and G. Pupillo, Supersolid droplet crystal in a dipole-blockaded gas, *Phys. Rev. Lett.* **105**, 135301 (2010).
- [37] G. Pupillo, A. Micheli, M. Boninsegni, I. Lesanovsky, and P. Zoller, Strongly correlated gases of rydberg-dressed atoms: Quantum and classical dynamics, *Phys. Rev. Lett.* **104**, 223002 (2010).
- [38] F. Maucher, N. Henkel, M. Saffman, W. Królikowski, S. Skupin, and T. Pohl, Rydberg-induced solitons: Three-dimensional self-trapping of matter waves, *Phys. Rev. Lett.* **106**, 170401 (2011).
- [39] B. Xiong, H. H. Jen, and D.-W. Wang, Topological superfluid by blockade effects in a rydberg-dressed fermi gas, *Phys. Rev. A* **90**, 013631 (2014).

- [40] X. Li and S. D. Sarma, Exotic topological density waves in cold atomic rydberg-dressed fermions, *Nature Communications* **6**, 7137 (2015).
- [41] Y.-Y. Jau, A. M. Hankin, T. Keating, I. H. Deutsch, and G. W. Biedermann, Entangling atomic spins with a rydberg-dressed spin-flip blockade, *Nature Physics* **12**, 71 (2016).
- [42] J. Zeiher, R. van Bijnen, P. S. S. Hild, T. P. Jae-yoon Choi, I. Bloch, and C. Gross, s, arXiv: 1602.06313 (2013).
- [43] S. Murakami, Phase transition between the quantum spin hall and insulator phases in 3d: emergence of a topological gapless phase, *New Journal of Physics* **9**, 356 (2007).
- [44] J. Honer, H. Weimer, T. Pfau, and H. P. Büchler, Collective many-body interaction in rydberg dressed atoms, *Phys. Rev. Lett.* **105**, 160404 (2010).
- [45] T. G. Walker and M. Saffman, Consequences of zeeman degeneracy for the van der waals blockade between rydberg atoms, *Phys. Rev. A* **77**, 032723 (2008).
- [46] K. Singer, M. Reetz-Lamour, T. Amthor, S. Fölling, M. Tschernneck, and M. Weidemüller, Spectroscopy of an ultracold rydberg gas and signatures of rydberg-rydberg interactions, *Journal of Physics B: Atomic, Molecular and Optical Physics* **38**, S321 (2005).
- [47] Y. Tanaka, Y. Mizuno, T. Yokoyama, K. Yada, and M. Sato, Anomalous andreev bound state in noncentrosymmetric superconductors, *Phys. Rev. Lett.* **105**, 097002 (2010).
- [48] M. Sato and S. Fujimoto, Existence of majorana fermions and topological order in nodal superconductors with spin-orbit interactions in external magnetic fields, *Phys. Rev. Lett.* **105**, 217001 (2010).
- [49] A. P. Schnyder and S. Ryu, Topological phases and surface flat bands in superconductors without inversion symmetry, *Phys. Rev. B* **84**, 060504 (2011).
- [50] A. Kitaev and J. Preskill, Topological entanglement entropy, *Phys. Rev. Lett.* **96**, 110404 (2006).
- [51] M. Levin and X.-G. Wen, Detecting topological order in a ground state wave function, *Phys. Rev. Lett.* **96**, 110405 (2006).
- [52] H. Li and F. D. M. Haldane, Entanglement spectrum as a generalization of entanglement entropy: Identification of topological order in non-abelian fractional quantum hall effect states, *Phys. Rev. Lett.* **101**, 010504 (2008).
- [53] F. Pollmann, A. M. Turner, E. Berg, and M. Oshikawa, Entanglement spectrum of a topological phase in one dimension, *Phys. Rev. B* **81**, 064439 (2010).
- [54] A. M. Turner, F. Pollmann, and E. Berg, Topological phases of one-dimensional fermions: An entanglement point of view, *Phys. Rev. B* **83**, 075102 (2011).
- [55] P.-Y. Chang, C. Mudry, and S. Ryu, Symmetry-protected entangling boundary zero modes in crystalline topological insulators, *Journal of Statistical Mechanics: Theory and Experiment* **2014**, P09014 (2014).
- [56] S. Ryu and Y. Hatsugai, Entanglement entropy and the berry phase in the solid state, *Phys. Rev. B* **73**, 245115 (2006).
- [57] M.-C. Chung, Y.-H. Jhu, P. Chen, and S. Yip, Edge states, entanglement entropy spectra and critical hopping couplings of anisotropic honeycomb lattices, *EPL (Europhysics Letters)* **95**, 27003 (2011).
- [58] M.-C. Chung, Y.-H. Jhu, P. Chen, and C.-Y. Mou, Quench dynamics of topological maximally entangled states, *Journal of Physics: Condensed Matter* **25**, 285601 (2013).
- [59] S. Matsuura, P.-Y. Chang, A. P. Schnyder, and S. Ryu, Protected boundary states in gapless topological phases, *New Journal of Physics* **15**, 065001 (2013).
- [60] N. Read and D. Green, Paired states of fermions in two dimensions with breaking of parity and time-reversal symmetries and the fractional quantum hall effect, *Phys. Rev. B* **61**, 10267 (2000).
- [61] H. Sumiyoshi and S. Fujimoto, Quantum thermal hall effect in a time-reversal-symmetry-broken topological superconductor in two dimensions: Approach from bulk calculations, *Journal of the Physical Society of Japan* **82**, 023602 (2013), <https://doi.org/10.7566/JPSJ.82.023602>.
- [62] K. Nomura, S. Ryu, A. Furusaki, and N. Nagaosa, Cross-correlated responses of topological superconductors and superfluids, *Phys. Rev. Lett.* **108**, 026802 (2012).
- [63] P.-Y. Chang, S. Matsuura, A. P. Schnyder, and S. Ryu, Majorana vortex-bound states in three-dimensional nodal noncentrosymmetric superconductors, *Phys. Rev. B* **90**, 174504 (2014).
- [64] J.-X. Yin, Z. Wu, J.-H. Wang, Z.-Y. Ye, J. Gong, X.-Y. Hou, L. Shan, A. Li, X.-J. Liang, X.-X. Wu, J. Li, C.-S. Ting, Z.-Q. Wang, J.-P. Hu, P.-H. Hor, H. Ding, and S. H. Pan, Observation of a robust zero-energy bound state in iron-based superconductor fe(te,se), *Nature Physics* **11**, 543 (2015).
- [65] A. Palacio-Morales, E. Mascot, S. Cocklin, H. Kim, S. Rachel, D. K. Morr, and R. Wiesendanger, Atomic-scale interface engineering of majorana edge modes in a 2d magnet-superconductor hybrid system, *Science Advances* **5**, 10.1126/sciadv.aav6600 (2019), <https://advances.sciencemag.org/content/5/7/eaav6600.full.pdf>.
- [66] S. M. Frolov, M. J. Manfra, and J. D. Sau, Topological superconductivity in hybrid devices, *Nature Physics* **16**, 718 (2020).
- [67] D. Wang, L. Kong, P. Fan, H. Chen, S. Zhu, W. Liu, L. Cao, Y. Sun, S. Du, J. Schneeloch, R. Zhong, G. Gu, L. Fu, H. Ding, and H.-J. Gao, Evidence for majorana bound states in an iron-based superconductor, *Science* **362**, 333 (2018), <https://science.sciencemag.org/content/362/6412/333.full.pdf>.
- [68] C. V. Kraus, S. Diehl, P. Zoller, and M. A. Baranov, Preparing and probing atomic majorana fermions and topological order in optical lattices, *New Journal of Physics* **14**, 113036 (2012).